Jump rope vortex in liquid metal convection

Tobias Vogt[a,b,1,2], Susanne Horn[a,1,2], Alexander M. Grannan[a], and Jonathan M. Aurnou[a]

[a]Department of Earth, Planetary, and Space Sciences, University of California, Los Angeles, CA 90095; and [b]Institute of Fluid Dynamics, Helmholtz-Zentrum Dresden-Rossendorf, 01328 Dresden, Germany

Edited by Friedrich Busse, Physikalisches Institut, Bayreuth, Germany, and approved October 19, 2018 (received for review July 17, 2018)

Understanding large-scale circulations (LSCs) in turbulent convective systems is important for the study of stars, planets, and in many industrial applications. The canonical model of the LSC is quasi-planar with additional horizontal sloshing and torsional modes [Brown E, Ahlers G (2009) *J Fluid Mech* 638:383–400; Funfschilling D, Ahlers G (2004) *Phys Rev Lett* 92:194502; Xi HD et al. (2009) *Phys Rev Lett* 102:044503; Zhou Q et al. (2009) *J Fluid Mech* 630:367–390]. Using liquid gallium as the working fluid, we show, via coupled laboratory-numerical experiments in tanks with aspect ratios greater than unity ($\Gamma \in \{\sqrt{2}, 2\}$), that the LSC takes instead the form of a "jump rope vortex," a strongly 3D mode that periodically orbits around the tank following a motion much like a jump rope on a playground. Further experiments show that this jump rope flow also exists in more viscous fluids such as water, albeit with a far smaller signal. Thus, this jump rope mode is an essential component of the turbulent convection that underlies our observations of natural systems.

thermal convection | turbulence | coherent structures | liquid metals

In fully turbulent convecting systems, convective energy coalesces into coherent, large-scale flows. These fluid motions manifest as superstructures in most geo- and astrophysical systems, where they form characteristic patterns such as the granulation on the sun's surface or cloud streets in the atmosphere (1–3). The underlying building block of these superstructures is a singular large-scale circulation (LSC), first observed over 35 years ago in the laboratory experiments of Krishnamurti and Howard (4). The LSC, also called the "wind of turbulence" (5), is the largest overturning structure in a given fluid layer. Despite the similar shape, the turbulent LSC is distinct from the laminar convection rolls that develop at convective onset (6–9). An agglomeration of LSCs can then act to form a superstructure in spatially extended fluid layers (1–3, 10, 11).

In all natural and experimental turbulent convecting fluid systems, LSCs have been found to exist (8, 12–17). They have been described as having a quasi-2D, vertical planar structure whose flow follows a roughly circular or elliptical path (7–9, 18, 19). Within contained systems, the quasi-planar flow rises vertically on one side of the container and descends vertically on the antipode. All LSCs have a regular low-frequency oscillation that is the dominant spectral signature of the flow (e.g., refs. 7, 12, 20–22). In recent years, this low-frequency oscillation has been characterized as arising from a misalignment of the vertical symmetry plane of the LSC, resulting in a horizontal sloshing and torsioning of the LSC flow (8, 9, 18, 19, 23, 24). In a decoupled view of the motions, the torsioning of the plane resembles a sheet of paper being alternately twisted and countertwisted around the central axis of the container, and the horizontal sloshing mode resembles a purely vertical sheet moving side-to-side through the fluid, perpendicular to the LSC plane. It is argued that these two oscillatory modes are coupled such that they exist simultaneously in any given system (9, 18, 19).

Often considered the most important dynamical attribute of thermal convection, the LSC flow shears the upper and lower boundary of the fluid layer (14). This shearing promotes the emission of new thermal plumes, which, in turn, helps to drive the mean wind. Many theoretical approaches rely on the LSC concept to predict key output quantities, such as the net convective heat and momentum transport (5, 25, 26). Hence, having an accurate description of the LSC structure and the complete range of possible dynamics is mandatory.

Laboratory-Numerical Convection Experiments

We study turbulent Rayleigh–Bénard convection (RBC), in which a fluid layer is heated from below and cooled from above. The system is defined by three nondimensional control parameters: the Rayleigh number $Ra = \alpha g \Delta H^3/(\kappa\nu)$, which describes the strength of the buoyancy forcing relative to thermal and viscous dissipative effects; the Prandtl number $Pr = \nu/\kappa$, which describes the thermophysical fluid properties; and the container's aspect ratio $\Gamma = D/H$. Here, α is the isobaric thermal expansion coefficient, ν is the kinematic viscosity, κ is the thermal diffusivity, g is the gravitational acceleration, Δ is the temperature drop across the fluid layer, D is the diameter, and H is the height of the convection tank.

We have carried out combined laboratory-numerical RBC experiments using gallium, a low $Pr \simeq 0.027$ liquid metal, as the working fluid. The fluid is contained within a $\Gamma = 2$ cylinder, the largest container in which a single LSC will form and in which the highest convective velocities are attained (2, 3, 10, 11). This experimental design, which elaborates on the liquid mercury investigation of Tsuji et al. (13) and departs from canonical $Pr \sim 1$, $\Gamma \sim 1$ studies, allows a sole LSC to develop in a maximally unconfined, strongly turbulent environment. Estimating the relative coherence length as $l_{coh}/H = 10\,Pr^{1/2}(Ra(Nu-1))^{-1/4}$ (27), we obtain $l_{coh}/H \leq 0.09$ for all cases investigated. This low value suggests a fully turbulent flow, which is further

Significance

The large-scale circulation (LSC) is the key dynamical feature of turbulent thermal convection. It is the underlying structure that shapes the appearance of geo- and astrophysical systems, such as the solar granulation or cloud streets, and the cornerstone of theoretical models. Our laboratory-numerical experiments reveal that the LSC can perform a fully 3D motion resembling a twirling jump rope. The discovery of this LSC mode implies that the currently accepted paradigm of a quasi-planar oscillating LSC needs to be augmented. Moreover, it provides an important link between studies in confined geometries used in experiments and simulations and the effectively unconfined fluid layers in natural settings where an agglomeration of LSCs forms larger patterns.

Author contributions: T.V., S.H., A.M.G., and J.M.A. designed research; T.V., S.H., and A.M.G. performed research; T.V., S.H., A.M.G., and J.M.A. analyzed data; and T.V., S.H., A.M.G., and J.M.A. wrote the paper.

The authors declare no conflict of interest.

This article is a PNAS Direct Submission.

[1]T.V. and S.H. contributed equally to this work.

[2]To whom correspondence may be addressed. Email: susannehorn@ucla.edu or t.vogt@hzdr.de.

This article contains supporting information online at www.pnas.org/lookup/suppl/doi:10.1073/pnas.1812260115/-/DCSupplemental.

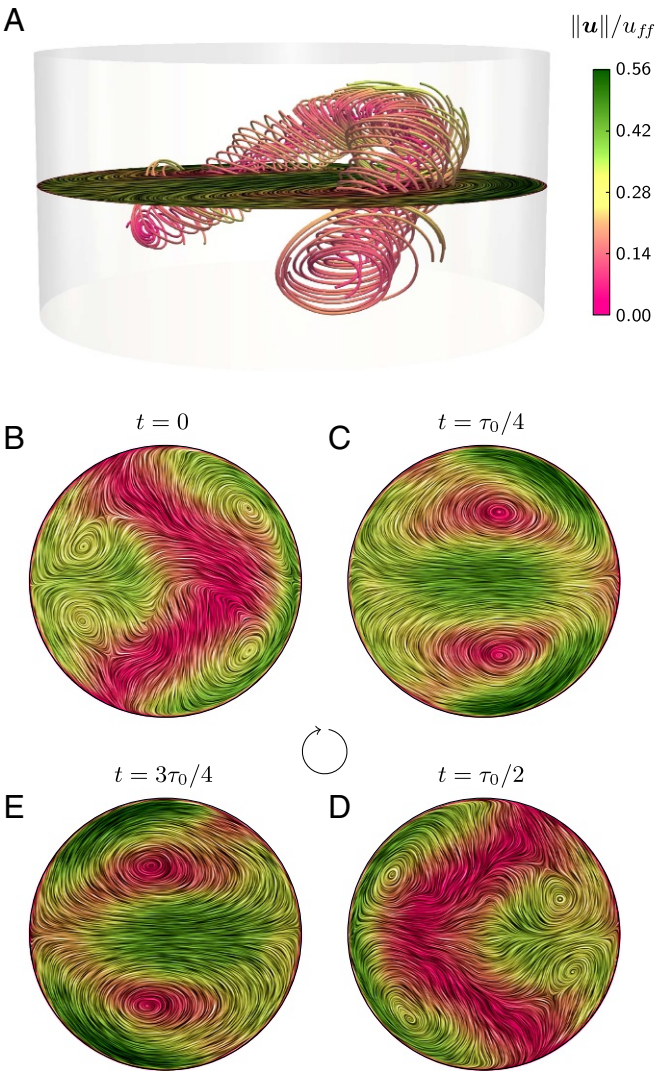

Fig. 1. The jump rope vortex. (*A*) A conditionally averaged 3D visualization of the streamlines at $t=\tau_0/4$ from DNS made with $Pr=0.025$, $Ra=1.12\times10^6$ in a cylindrical tank with a diameter-to-height aspect ratio $\Gamma=D/H=2$. The streamlines surround the jump rope vortex core, with streamline color denoting local velocity magnitude. In addition, in the midplane slice, color contours denote velocity magnitude and velocity streamlines are visualized by the line-integral convolution (LIC) method. The jump rope cycle is shown in $B\rightarrow C\rightarrow D\rightarrow E\rightarrow B$. Shown are cross-sections at half height, for the same conditionally averaged phases as the colored sidewall profiles in Fig. 4*B*. The vortex core of the LSC has minimal velocity (pink). In *B*, $t=\tau_0$, and *D*, $t=\tau_0/2$, the LSC is confined to the midplane. In *C*, $t=\tau_0/4$, and *E*, $t=3\tau_0/4$, the LSC has moved out of the midplane. The highest velocities (green) in *C*/*E* also show the clear splitting of the up- and downwelling flows (see *SI Appendix*, Movies S3–S4 and Fig. S1 for 3D renderings of *B*–*D*).

corroborated by relatively high Reynolds numbers $Re_{r,rms}>1.2\times10^3$ (see *SI Appendix*, Table S1). On the other hand, the Peclet number $Pe=Re\,Pr\leq250$ remains low (cf. ref. 28), resulting in larger, more coherent thermal signals than in moderate Pr fluids at a comparable turbulence level.

The large amplitude velocity and temperature signatures in our system enable us to detect and quantify modes of the LSC that have not been observed in the canonical set-up. In fact, we find a mode of large-scale turbulent convection with a 3D oscillation that deviates from the quasi-planar description of LSC motion (Fig. 1). Instead of sloshing or twisting side-to-side motions, our results show a flow that circulates around a crescent-shaped vortex, which in turn orbits the tank in the direction opposite the fluid velocity. As seen in *SI Appendix*, Movies S3 and S4, this vortex looks like a twirling jump rope.

Our $\Gamma=2$ liquid gallium laboratory experiments are performed on the RoMag device (see *Materials and Methods*) and span a Rayleigh number range of $7.1\times10^4\leq Ra\leq5.1\times10^6$. Ultrasonic Doppler velocimetry (29) is used to measure the instantaneous flow distribution along four different measuring lines (Fig. 2). Two ultrasonic transducers are attached antipodaly to the upper end block at cylindrical radius $r/R=2/3$ to measure the vertical velocity field (Fig. 2 *A* and *B*). Another two transducers are fixed to the sidewall horizontally at height $z/H=1/2$ to measure midplane velocities along the diameter (Fig. 2*C*) and along a chord (Fig. 2*D*). The transducers are all oriented to align approximately with the symmetry plane of the large-scale flow, except for the chord probe that is perpendicular to it. Additionally, 29 thermistors are used to measure the experimental temperature field, including the central temperature of the bulk fluid, the vertical temperature difference across the fluid layer, and along one-third of the midplane sidewall. With this set-up, we diagnose the 3D dynamics of the liquid metal LSC.

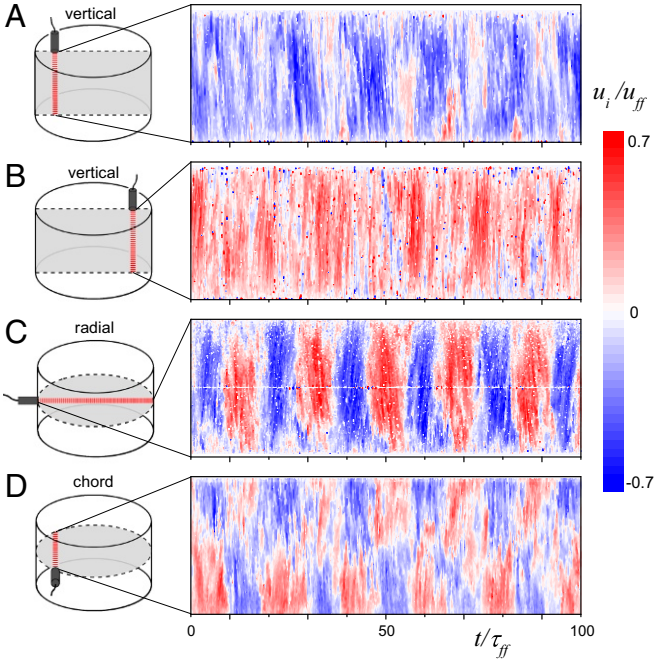

Fig. 2. Spatiotemporal evolution of laboratory convection velocities. Simultaneous ultrasonic Doppler measurements for the case at $Pr=0.027$, $Ra=1.03\times10^6$, and $\Gamma=2$. The particular measuring lines are indicated as a dashed red line in the schematics left of each data panel. Negative (positive) velocities represent flow away from (toward) the transducer. The measurements are nondimensionalized using the free-fall velocity $u_{ff}=\sqrt{\alpha g\Delta H}=21.95$ mm/s and the free-fall time $\tau_{ff}=H/u_{ff}=4.48$ s. The ordinate corresponds to the measuring depth along the tank height (*A* and *B*), diameter (*C*), and chord (*D*), respectively. The measurements in *A*–*C* lie in the symmetry plane of the LSC; the chord probe measurements in *D* lie perpendicular to the LSC symmetry plane. The axial velocity in *A* and *B* show a mean down- and upflow, respectively, and relatively weak periodic fluctuations. While the mean velocity is zero in *C* and *D*, strong oscillations are observed that span the tank. The flow along the chord in *D* shows a periodic double-cell structure whereby the oscillation is in phase to *C*. The strong periodic oscillation in *C* and *D* cannot be explained via the current LSC paradigm. (The white horizontal stripe in *C* is due to the standing echo from the 1-mm-diameter center-point thermistor.) The characteristic patterns are present in the entire investigated Rayleigh number range, $7.05\times10^4\leq Ra\leq5.14\times10^6$ (see *SI Appendix*, Fig. S2).

All of our ultrasonic Doppler results exhibit a distinctive velocity pattern, visualized in Fig. 2 for $Ra = 1.03 \times 10^6$. The vertical velocities in Fig. 2 *A* and *B* show flow near the axial plane of the LSC, with *A* representing the cold downwelling flow (blue) and *B* representing the warm upwelling motions (red) of the LSC. In addition, our measurements reveal both high- and low-frequency oscillations within the vertical velocity fields. The higher frequency oscillations correspond to small-scale plumes, whereas the lower frequency signals correspond to the fundamental oscillatory modes of the LSC. These vertical velocity measurements are in agreement with the quasi-planar model of the LSC. However, we find that the low-frequency oscillation is strongest in the horizontal direction, aligned along the LSC's horizontal midplane (Fig. 2*C*). Further, the midplane chord probe measurements (Fig. 2*D*) show that the horizontal velocity switches sign across the midpoint of the chord, which lies in the symmetry plane of the LSC. These data indicate that the fluid is periodically diverging from the axial LSC plane and then converging back toward it. The measured velocities approach the free-fall velocity (30) $u_{ff} = \sqrt{\alpha g \Delta H}$. These velocities are well within our measurement capabilities and are thus detected as robust features of the flow. Significantly, these diverging–converging chord-probe flows indicate the presence of a strongly 3D flow pattern that is inconsistent with either horizontal sloshing or torsional modes (18, 19) and, thus, requires a novel physical explanation.

To diagnose the modes of behavior of the inertial LSC flow within the opaque liquid metal, we carried out high-resolution direct numerical simulations (DNS), using the fourth order finite volume code GOLDFISH, to provide detailed information on the spatially and temporally fully resolved 3D temperature and velocity fields (see *Materials and Methods*). The main DNS uses parameter values of $\Gamma = 2$, $Ra = 1.12 \times 10^6$, and $Pr = 0.025$ and is run for 1,000 free-fall time units after reaching statistical equilibrium.

We compare the outputs from the DNS and the laboratory experiments in Fig. 3. Measuring velocities and temperatures near the central point of the fluid bulk, the spectral peak frequencies f_0 all agree to within 3.3% (Fig. 3 *A–D* and *SI Appendix*, Table S1). This quantitative agreement demonstrates that our DNS captures the essential behaviors of the laboratory experiments and is well-suited as a diagnostic tool to interpret the flows existing in the opaque liquid metal. In addition, the agreement shows that the idealized boundary conditions available in the DNS are sufficiently replicated in the laboratory experiments.

The value of f_0 is connected to the characteristic velocity of the LSC (Fig. 3 *E* and *F*) and thus to the momentum transport (5, 12, 31, 32). This transport is expressed by the Reynolds number Re—that is, $f_0 H^2/\kappa = cRePr$, with a constant c determined by the geometry. By linear regression of our dataset, we find that $f_0 \propto Ra^{0.419\pm0.006}$ or, equivalently (32), $Re \propto Ra^{0.433\pm0.006}$ (Fig. 3*E*). The frequency scaling exponent agrees with those obtained in the liquid metal, $\Gamma = 1$ experiments of Cioni et al. (12) and Schumacher et al. (14). Alternatively, the Reynolds number based on the rms value of the radial velocity data at the midpoint yields a slightly different scaling, $Re_{r,rms} \equiv u_{r,rms} D/\nu \propto Ra^{0.483}$ (Fig. 3*F*). The best fit to the Grossmann–Lohse model (31, 32), which assumes a characteristic mean velocity of the LSC, predicts an effective scaling of $Re \propto Ra^{0.435\pm0.002}$ corresponding to $f_0 \propto Ra^{0.422\pm0.002}$ over our parameter range. Thus, our DNS and experimental results are in agreement with time-averaged, kinematic models of LSC-dominated convective flows (5) but broaden the understanding of the time-varying LSC dynamics.

Similar to previous studies, we characterize the LSC via temperature measurements acquired along the midplane circumference of the cylinder (9, 19, 24, 33). These sidewall temperature measurements provide information about the large-scale convective flows in the interior of the convection cell. Because of the high thermal diffusivity of liquid metals, the large-scale temperature signal is exceptionally clear as the small-scale temperatures are damped by diffusion. In addition, the high velocities in inertial liquid metal convective flows strongly advect the large-scale temperature field, producing midplane temperatures that almost reach the imposed maximal temperatures that exist on the top and bottom boundaries. Thus, temperature signals provide a strong and clear window into the LSC dynamics in liquid metal flows.

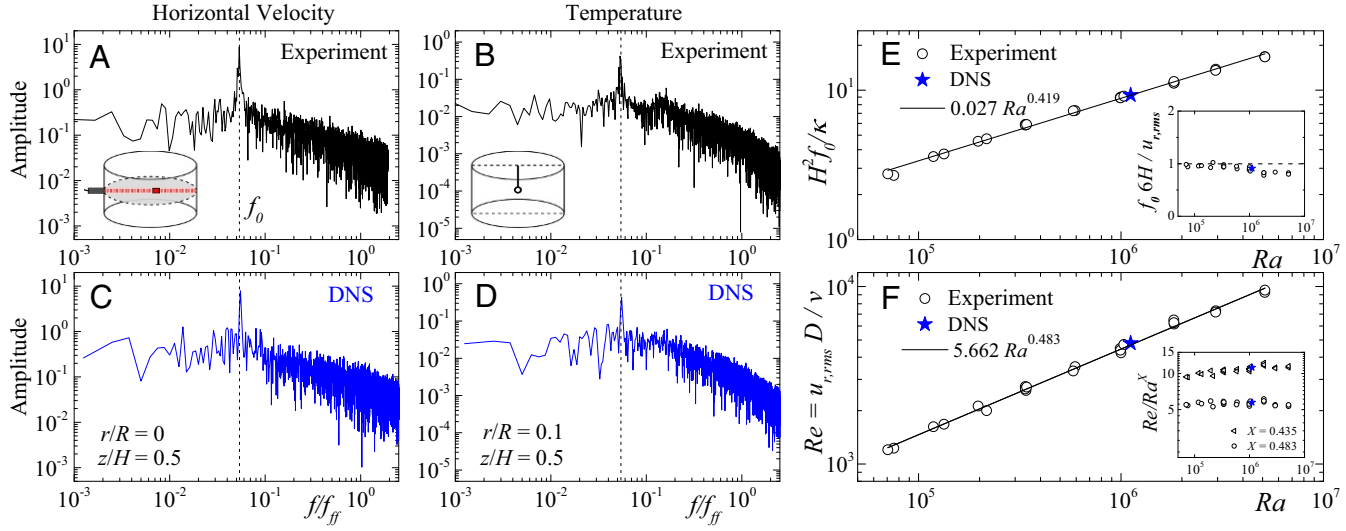

Fig. 3. Characteristic frequency and its scaling. Measured velocity and temperature frequency spectra in *A* and *B*, respectively, in laboratory data at $Ra = 1.03 \times 10^6$ and in *C* and *D* from DNS with $Ra = 1.12 \times 10^6$. All spectra are calculated using data obtained near the center of the fluid domain. The four dashed lines in *A–D* indicate f_0 taken from *A*. (*E*) The dominant frequency as a function of *Ra*, normalized by the thermal diffusion time, H^2/κ, for experiments (open circles) and DNS (blue star). The best fit of the experimental data yields $f_0 H^2/\kappa = 0.027 Ra^{0.419}$. The *Inset* shows the frequency normalized by the estimated LSC turnover time, $6H/u_{r,rms}$, where we use the maximum possible path length of $2H + 2D = 6H$. (*F*) The midpoint horizontal Reynolds number $Re_{r,rms}$ as a function of *Ra*, which varies as $5.662 Ra^{0.483}$. The Reynolds number compensated by our best fit $Re \propto Ra^{0.483}$ (circles) and by the effective Grossmann–Lohse scaling $Re \propto Ra^{0.435}$ (triangles) is in the *Inset*.

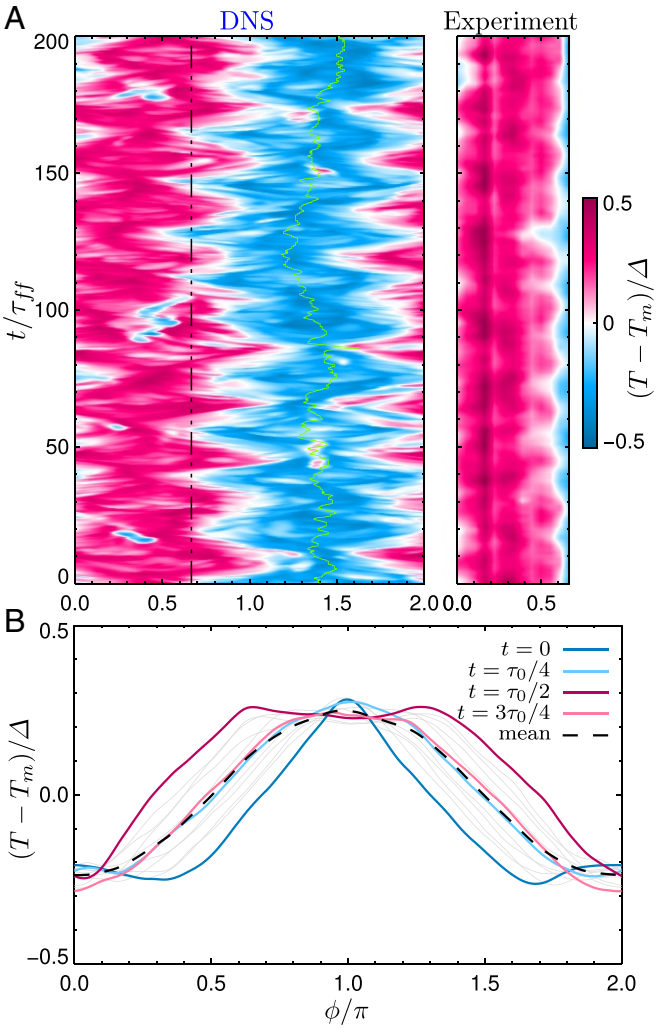

Fig. 4. Midplane temperature signal on the sidewall. (*A*) Numerically and experimentally obtained temperature $(T-T_m)/\Delta$ at half height shown for 200 free-fall time units t/τ_{ff} (also see *SI Appendix*, Figs. S3 and S4). The black dash-dotted line indicates the azimuthal ϕ-width covered by the thermocouple array in the laboratory experiment. The instantaneous position of the LSC ξ_{LSC} is demarcated by the green line, which exhibits relatively small meanderings. In contrast, the jump roping of the LSC causes the thermal pattern to fluctuate strongly, with warmer fluid (then colder fluid) occupying between one-third and two-thirds of the circumference, creating what looks like the baffles of an accordion. (*B*) Conditionally averaged DNS profiles of the temperature sidewall for the 12 phases of the jump rope oscillation. They reveal the splitting of the cold LSC downflow at $t=0$ (dark blue) and hot LSC upflow at $t=\tau_0/2$ (dark magenta) by clear double minima and maxima, respectively. The disparity of the profiles at $t=\tau_0/4$ (light blue) and $t=3\tau_0/4$ (light magenta) suggests that the motion is 3D. The gray lines are the profiles for the remaining eight phases of the oscillation. The total mean (black dashed line) results in a simple cosine function.

Jump Rope Vortex Cycle

Fig. 4*A* shows the midplane sidewall temperatures in the DNS (*Left*) at $Ra=1.12\times10^6$ and in the laboratory experiment (*Right*) at $Ra=1.03\times10^6$. The distinct blue and pink regions (cold and hot, respectively) reveal strong temperature alternations within the fluid, which we call an accordion pattern. At $t/\tau_{ff}=0$, the cold fluid covers roughly two-thirds of the sidewall circumference; by $t/\tau_{ff}\simeq10$, the cold fluid covers only one-third of the circumference and then subsequently expands in azimuth again. Averaging the sidewall temperatures over the entire circumference, $T_{avg}=\langle T(r=R,z=H/2)\rangle_\phi$, consequentially yields quasi-periodic oscillations in T_{avg} (see *Materials and Methods*). Unlike cases dominated by torsion and sloshing modes (8, 9, 18, 19), our sidewall measurements have the same frequency f_0 as found in the central measurements shown in Fig. 3 *A–D*. The accordion pattern in the sidewall temperatures (Fig. 4*A* and *SI Appendix*, Figs. S3 and S4) and the corresponding oscillation in T_{avg} (Fig. 5) provide the simplest means for identifying the jump rope mode in convection data.

To fully diagnose the 3D characteristics of the LSC in the DNS, we first determined the position of the LSC within the fluid domain for each snapshot. Extending the single-sinusoidal fitting method of Cioni et al. (12) and Brown et al. (33), each snapshot's midplane sidewall temperature distribution is fit to the function

$$T_{fit}(\phi)=a\cos(\phi-\xi_{LSC})+b\cos(2(\phi-\xi_{LSC}))+T_{avg}, \quad [1]$$

where ξ_{LSC} denotes the symmetry plane of the LSC (i.e., the green line in Fig. 4*A* and *SI Appendix*, Movie S1). The values of a and b give the relative amplitudes of the hot and cold sidewall signals.

For $\Gamma=2$, there is a strong quasi-periodic temporal oscillation in the T_{avg} signal with frequency f_0 (see *Materials and Methods* and Fig. 5), however we do not find a pronounced oscillation in the azimuthal angle ξ_{LSC} (see Fig. 4*A*). The frequency f_0 agrees with the ones determined from the spectra presented in Fig. 3 *A–D*. This behavior differs strongly from measurements conducted in $\Gamma\sim1$ vessels (e.g., refs. 8, 14, 18, 34, 35), where the temporal oscillation exists in the azimuthal orientation angle ξ_{LSC} and corresponds to a horizontal sloshing (see *SI Appendix*, Fig. S3 for a juxtaposition of $\Gamma=2$ and $\Gamma=1$ results). Irrespective of the Γ value, temperature and velocity spectral measurements exhibit a low frequency peak. Brown and Ahlers (18) and Xi et al. (19) interpret the low frequency peak in the spectrum of the second Fourier moment (b of ref. 1) as the signature of a horizontal slosh. In contrast, we also find a significant low-frequency variability in b due to the jump rope mode. This then implies that spectra alone are insufficient to draw inferences on the flow morphology of the LSC.

We decompose the oscillation period $\tau_0=1/f_0$ into 12 phases based on the rms value of the sidewall midplane temperature. Using these 12 phases, 10,000 temporally equidistant snapshots are conditionally averaged over a total time span of $t/\tau_{ff}=1{,}000$. In this operation, we first orient the solution so that the LSC symmetry plane remains fixed in azimuth and then average the temperature and velocity fields at the same temporal phase values, as shown in *SI Appendix*, Movie S2.

Our 12 conditionally averaged midplane, sidewall temperature profiles are shown in Fig. 4*B*. In agreement with previous quasi-planar LSC studies, the average of all phases yields a cosine

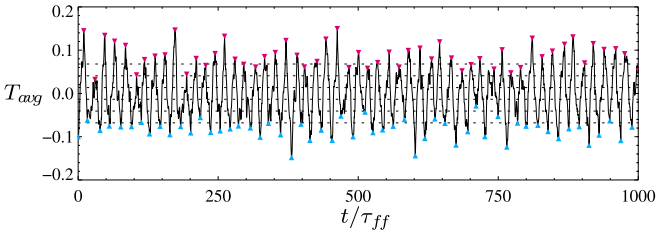

Fig. 5. Circumferentially averaged temperature signal at midheight T_{avg} from DNS with $Pr=0.025$, $Ra=1.12\times10^6$, and $\Gamma=2$. The magenta (blue) downward (upward) triangles mark the hand-selected maxima (minima). The horizontal dashed lines correspond to multiples of the SDσ of T_{avg}, given by $\pm\frac{n}{4}\sigma$, $n\in\{1,3,5\}$, by which we separated the conditional averaging intervals. The oscillation frequency of the signal matches f_0 as obtained at the center point, shown in Fig. 3, and is one of the most accessible identification schemes for the jump rope vortex.

function (dashed black line). However, our conditional averaging also reveals a more complex thermal structure with three extrema in the $t=0$ and $t=\tau_0/2$ profiles, with either a double maxima–single minimum or double minima–single maximum structure. Thus, our conditional averaging extracts information about the presence of additional complexity within the LSC dynamics. Further, a pure cosine function is not present at $t=\tau_0/4$ and $t=3\tau_0/4$, requiring the existence of spatiotemporal complexity in the LSC flow field.

The convective flow can only be understood by considering the LSC as a fully 3D vortical structure, whose vortex core traces a path similar to that of a jump rope that precesses around the tank in the direction opposite that of the LSC flow itself. The motion of the jump rope vortex is illustrated by the streamlines that circumscribe the vortex core in Fig. 1. At the center of the vortex (pink hörnchen-like structure), the velocity magnitude is zero. As viewed in *SI Appendix*, Movie S2 and S4 as well as in *SI Appendix*, Fig. S1, the LSC fluid motions are in the clockwise direction, whereas the motion of the LSC core is counterclockwise, akin to a planetary gear.

Looking in detail at the jump rope vortex cycle, we find at $t=0$ that the LSC core is restricted to the horizontal midplane $z=H/2$ (Fig. 1*B*). At this time, the vortex core nears the midplane sidewall, impinging on the cold downwelling flow that exists there. This splits the downwelling fluid into two branches, creating the two distinct minima in the $t=0$ midplane temperature profile (Fig. 4*B*). The splitting motions generate horizontally divergent flows, which explain the chord probe measurements of the experimental velocity field (Fig. 2*D*). By necessity, on the other side of the tank, the warm upwelling flow gets collimated, creating a high-pressure wave along the bottom boundary layer. We hypothesize this collimation promotes the generation of instabilities and thereby the detachment of warm convective plumes that drive the LSC more vigorously in the lower half of the cylinder, mainly along the ξ_{LSC} plane, and push the center of the LSC upward, initiating a broadening of the warm upwelling.

We find at $t=\tau_0/4$ (Fig. 1 *A* and *C*) that the vortex core no longer impinges on the midplane but has moved to the upper half of the tank and the LSC has stretched to its longest elliptical path length. At this point, the cold downflow is still split, but the midplane temperature extrema are less pronounced. We find mirrored motions at $\tau=0$ and $\tau=\tau_0/2$ and similarly at $\tau=\tau_0/4$ and $\tau=3\tau_0/4$, thereby producing a symmetrical jump rope cycle (Fig. 1 *B*–*D*).

Summary and Discussion

We have verified that the observed jump rope behavior is not unique to thermal convection in small Pr fluids by simulating water with $Pr=4.38$ and $Ra=10^8$ (see *SI Appendix*, Fig. S3). A coarse conditional-averaging scheme shows that the fundamental jump rope mode is detectable for $\Gamma=2$. The oscillation frequency is much lower in this fluid, and the thermal and kinematic flow fields are both equally turbulent so that the sidewall temperature signals are far less pronounced (see *SI Appendix*).

Our results complement the fundamental view of LSCs. Based on our combined laboratory-numerical experiments, we find that the LSC in a $\Gamma\geq\sqrt{2}$ container is not confined to a quasi-2D circulation plane perturbed by 3D twisting and horizontal sloshing modes. Instead, we find the LSC has a dominant 3D vortex core that travels in a fully 3D jump rope-like motion in the direction opposite to that of the LSC flow field. Determining the range of Γ over which this solution dominates still requires elucidation. We further hypothesize that additional 3D modes exist within the LSC framework. Advanced techniques [e.g., dynamic mode decomposition (36), Koopman filtering (37)] will eventually reveal the full dynamics underlying turbulent convection in effectively unconfined systems.

Materials and Methods

Laboratory Setup. The experiments were performed with the RoMag device (38, 39) using the liquid metal gallium confined in a right cylinder of aspect ratio $\Gamma=D/H=2$ with diameter $D=196.8$ mm and height $H=98.4$ mm. The container's sidewall is made of stainless steel, while the endwalls are made of copper. A noninductively wound heater provides a heating power between 6 W and 1,600 W at the bottom copper endwall. This heat is removed by a thermostated bath that circulates water through a double wound heat exchanger located above the top endwall. The sidewalls are wrapped by a 20-mm layer of closed-cell foam insulation, followed by 30 mm of Insulfrax fibrous thermal blanketing and a 30-mm layer of closed-cell foam insulation to minimize radial heat losses.

Twenty-three experiments were conducted where the range of mean fluid temperatures varied between $35\,^\circ\text{C}\leq T_m\leq 47\,^\circ\text{C}$ and the temperature drop across the fluid layer between $0.28\leq\Delta\leq 19.36\,K$. Using the material properties for gallium (40), the Prandtl number ranges between $0.026\leq Pr\leq 0.028$ and the Rayleigh number between $7.1\times10^4\leq Ra\leq 5.1\times10^6$. Ultrasound Doppler velocimetry is used to measure the instantaneous velocity distribution along four different measuring lines, as shown in Fig. 2. This technique is useful for measuring the velocities in opaque fluids noninvasively (29, 41, 42). The transducers (TR0805SS, Signalprocessing SA) capture the velocity component parallel to their ultrasound beam with resolutions of about 1 mm in space and 1 Hz in time. All transducers are in direct contact with the liquid metal. They are approximately oriented in the LSC symmetry plane, except for the chord probe that is perpendicular to it.

A total of 29 thermocouples are used to monitor the temperatures in the experiment. Six thermistors are embedded in each of the copper endwalls 2 mm away from the fluid layer and are used to determine T_m and Δ. Seven thermistors are distributed inside the fluid layer, while 15 thermocouples are placed around the perimeter outside the fluid volume at midheight $z/H=0.5$. Thirteen of those thermocouples are positioned in an array 10 degrees apart and used in the experimental array in Fig. 4*A*. The temporal resolution of the thermal measurements is 10 Hz. Experiments are conducted until equilibration is reached, when the thermal signals vary by less than 1% over 30 min. Data are then saved for between three and six thermal diffusion times. In postprocessing, thermocouples placed between the insulation layers provide an estimate for sidewall heat losses. Additionally, the heat losses through vertical conduction in the stainless steel sidewall are also accounted for, and the top and bottom fluid temperatures are corrected to include the conduction in the copper endways.

DNS. The DNS have been conducted with the fourth-order accurate finite volume code GOLDFISH (26, 36, 43). It numerically solves the nondimensional Navier–Stokes equations in the Oberbeck–Boussinesq approximation augmented by the temperature equation in a cylindrical (r, ϕ, z) domain:

$$\vec{\nabla}\cdot\vec{u}=0, \quad [2]$$

$$D_t\vec{u}=Ra^{-\frac{1}{2}}Pr^{\frac{1}{2}}\gamma^{-\frac{3}{2}}\vec{\nabla}^2\vec{u}-\vec{\nabla}p+T\hat{\vec{e}}_z, \quad [3]$$

$$D_tT=Ra^{-\frac{1}{2}}Pr^{-\frac{1}{2}}\gamma^{-\frac{3}{2}}\vec{\nabla}^2T, \quad [4]$$

where γ is the radius-to-height aspect ratio $R/H=\Gamma/2$. The radius R, the buoyancy velocity $(g\alpha R\Delta)^{1/2}$, the temperature difference Δ, and the material properties at T_m are used as the reference scales. The mechanical boundary conditions are no-slip on all solid walls, and the temperature boundary conditions are isothermal for the top and bottom and perfectly insulating for the sidewalls.

The numerical resolution for the main DNS with $Pr=0.025$, $Ra=1.12\times10^6$, $\Gamma=2$ is $N_r\times N_\phi\times N_z=168\times171\times168$; the total run-time was 1,000 free-fall time units after reaching a statistical steady state. The obtained results were verified on a finer $280\times256\times280$ mesh. In addition, DNS for the same Pr and Ra were also carried out with a smaller aspect ratio of $\Gamma=\sqrt{2}$ for $t=100\tau_{ff}$ and $\Gamma=1$ for $t=500\tau_{ff}$. For $\Gamma=\sqrt{2}$, the dominant LSC motion is a jump rope, whereas for $\Gamma=1$, it is the well-studied combination of sloshing and twisting motions. The Γ dependence of the dominant LSC mode was also confirmed in moderate-Pr fluids by means of DNS with $Pr=4.38$ and $Ra=10^8$ and aspect ratios $\Gamma\in\{1,2\}$ with run times of $t=1414\tau_{ff}$ and $t=612\tau_{ff}$, respectively (see *SI Appendix*, Figs. S3 and S4).

Conditional Averaging. The temperature signal $T_{avg}=\langle T(r=R,z=H/2)\rangle_\phi$—that is, the sidewall temperature at midheight averaged in azimuthal direction—shows a distinct oscillation with frequency f_0, shown

in Fig. 5. To extract the characteristic behavior during one cycle, we have sampled 10 snapshots per time unit, resulting in a total of 10,000 snapshots. We then defined seven intervals based on the SDσ of T_{avg} by the boundaries $-\frac{5}{4}\sigma$, $-\frac{3}{4}\sigma$, $-\frac{1}{4}\sigma$, $\frac{1}{4}\sigma$, $\frac{3}{4}\sigma$, $\frac{5}{4}\sigma$. For $|T_{avg}| > \frac{5}{4}\sigma$, all snapshots in those intervals were averaged. In the remaining intervals, we additionally considered whether the signal was in a phase where the temperature increases or decreases, respectively. This was algorithmically achieved by determining if the snapshot was located between a maximum and minimum or between a maximum and minimum. However, due to the possible occurrence of several multiple local extrema during one cycle, we had to hand-select the maxima and minima as shown in Fig. 5. The results were 12 averaging intervals.

ACKNOWLEDGMENTS. We thank two anonymous referees and the editor for their constructive feedback. This work was supported by NSF Geophysics Program Award 1547269. T.V. acknowledges the Helmholtz Association for financial support within the framework of the Helmholtz-Alliance Liquid-Metal Technology (LIMTECH) and for supporting his stay in Los Angeles. S.H. acknowledges funding by the German Research Foundation (DFG) under Grant HO 5890/1-1 and Leibniz-Rechenzentrum for providing computational resources on SuperMUC.

1. Von Hardenberg J, Parodi A, Passoni G, Provenzale A, Spiegel EA (2008) Large-scale patterns in Rayleigh–Bénard convection. *Phys Lett A* 372:2223–2229.
2. Pandey A, Scheel JD, Schumacher J (2018) Turbulent superstructures in Rayleigh-Bénard convection. *Nat Comm* 9:2118.
3. Stevens RJ, Blass A, Zhu X, Verzicco R, Lohse D (2018) Turbulent thermal superstructures in Rayleigh-Bénard convection. *Phys Rev Fluids* 3:041501.
4. Krishnamurti R, Howard LN (1981) Large-scale flow generation in turbulent convection. *Proc Natl Acad Sci USA* 78:1981–1985.
5. Grossmann S, Lohse D (2000) Scaling in thermal convection: A unifying theory. *J Fluid Mech* 407:27–56.
6. Xi H-D, Lam S, Xia K-Q (2004) From laminar plumes to organized flows: The onset of large-scale circulation in turbulent thermal convection. *J Fluid Mech* 503: 47–56.
7. Villermaux E (1995) Memory-induced low frequency oscillations in closed convection boxes. *Phys Rev Lett* 75:4618–4621.
8. Funfschilling D, Ahlers G (2004) Plume motion and large-scale circulation in a cylindrical Rayleigh-Bénard cell. *Phys Rev Lett* 92:194502.
9. Zhou Q, Xi H-D, Zhou S-Q, Sun C, Xia K-Q (2009) Oscillations of the large-scale circulation in turbulent Rayleigh–Bénard convection: The sloshing mode and its relationship with the torsional mode. *J Fluid Mech* 630:367–390.
10. Sakievich PJ, Peet YT, Adrian RJ (2016) Large-scale thermal motions of turbulent Rayleigh–Bénard convection in a wide aspect-ratio cylindrical domain. *Int J Heat Fluid Flow* 61:183–196.
11. Bailon-Cuba J, Emran MS, Schumacher J (2010) Aspect ratio dependence of heat transfer and large-scale flow in turbulent convection. *J Fluid Mech* 655:152–173.
12. Cioni S, Ciliberto S, Sommeria J (1997) Strongly turbulent Rayleigh–Bénard convection in mercury: Comparison with results at moderate Prandtl number. *J Fluid Mech* 335:111–140.
13. Tsuji Y, Mizuno T, Mashiko T, Sano M (2005) Mean wind in convective turbulence of mercury. *Phys Rev Lett* 94:034501.
14. Schumacher J, Bandaru V, Pandey A, Scheel JD (2016) Transitional boundary layers in low-Prandtl-number convection. *Phys Rev Fluids* 1:084402.
15. Horn S, Shishkina O (2015) Toroidal and poloidal energy in rotating Rayleigh–Bénard convection. *J Fluid Mech* 762:232–255.
16. Horn S, Shishkina O, Wagner C (2013) On non-Oberbeck–Boussinesq effects in three-dimensional Rayleigh–Bénard convection in glycerol. *J Fluid Mech* 724:175–202.
17. Breuer M, Hansen U (2009) Turbulent convection in the zero Reynolds number limit. *Europhys Lett* 86:24004.
18. Brown E, Ahlers G (2009) The origin of oscillations of the large-scale circulation of turbulent Rayleigh–Bénard convection. *J Fluid Mech* 638:383–400.
19. Xi H-D, Zhou S-Q, Zhou Q, Chan T-S, Xia K-Q (2009) Origin of the temperature oscillation in turbulent thermal convection. *Phys Rev Lett* 102:044503.
20. Heslot F, Castaing B, Libchaber A (1987) Transitions to turbulence in helium gas. *Phys Rev A* 36:5870–5873.
21. Castaing B, Gunaratne G, Kadanoff L, Libchaber A, Heslot F (1989) Scaling of hard thermal turbulence in Rayleigh–Bénard convection. *J Fluid Mech* 204:1–30.
22. Ciliberto S, Cioni S, Laroche C (1996) Large-scale flow properties of turbulent thermal convection. *Phys Rev E* 54:R5901–R5904.
23. Sun C, Xia K-Q, Tong P (2005) Three-dimensional flow structures and dynamics of turbulent thermal convection in a cylindrical cell. *Phys Rev E* 72:026302.
24. Stevens RJAM, Clercx HJH, Lohse D (2011) Effect of plumes on measuring the large scale circulation in turbulent Rayleigh-Bénard convection. *Phys Fluids* 23:095110.
25. Ahlers G, Grossmann S, Lohse D (2009) Heat transfer and large scale dynamics in turbulent Rayleigh-Bénard convection. *Rev Mod Phys* 81:503–537.
26. Shishkina O, Horn S, Wagner S, Ching ESC (2015) Thermal boundary layer equation for turbulent Rayleigh-Bénard convection. *Phys Rev Lett* 114:114302.
27. Sugiyama K, Calzavarini E, Grossmann S, Lohse D (2007) Non–Oberbeck-Boussinesq effects in two-dimensional Rayleigh-Bénard convection in glycerol. *EPL* 80:34002.
28. Grossmann S, Lohse D (2008) Thermal convection in small Prandtl number liquids: Strong but ineffective. *AIP Conference Proceedings* 1076:68–75.
29. Vogt T, et al. (2018) Transition between quasi-two-dimensional and three-dimensional Rayleigh-Bénard convection in a horizontal magnetic field. *Phys Rev Fluids* 3:013503.
30. Glazier JA, Segawa T, Naert A, Sano M (1999) Evidence against 'ultrahard' thermal turbulence at very high Rayleigh numbers. *Nature* 398:307–310.
31. Stevens RJAM, van der Poel EP, Grossmann S, Lohse D (2013) The unifying theory of scaling in thermal convection: The updated prefactors. *J Fluid Mech* 730:295–308.
32. Grossmann S, Lohse D (2002) Prandtl and Rayleigh number dependence of the Reynolds number in turbulent thermal convection. *Phys Rev E* 66:16305, ISSN 1550-2376.
33. Brown E, Nikolaenko A, Ahlers G (2005) Reorientation of the large-scale circulation in turbulent Rayleigh-Bénard convection. *Phys Rev Lett* 95:084503.
34. Resagk C, et al. (2006) Oscillations of the large scale wind in turbulent thermal convection. *Phys Fluids* 18:095105.
35. Xi H-D, Zhou Q, Xia K-Q (2006) Azimuthal motion of the mean wind in turbulent thermal convection. *Phys Rev E* 73:056312.
36. Horn S, Schmid PJ (2017) Prograde, retrograde, and oscillatory modes in rotating Rayleigh–Bénard convection. *J Fluid Mech* 831:182–211.
37. Giannakis D, Kolchinskaya A, Krasnov D, Schumacher J (2018) Koopman analysis of the long-term evolution in a turbulent convection cell. *J Fluid Mech* 847:735–767.
38. King EM, Stellmach S, Aurnou JM (2012) Heat transfer by rapidly rotating Rayleigh–Bénard convection. *J Fluid Mech* 691:568–582.
39. King EM, Aurnou JM (2013) Turbulent convection in liquid metal with and without rotation. *Proc Natl Acad Sci USA* 110:6688–6693.
40. Aurnou JM, Bertin V, Grannan AM, Horn S, Vogt T (2018) Rotating thermal convection in liquid gallium: Multi-modal flow, absent steady columns. *J Fluid Mech* 846:846–876.
41. Vogt T, Grants I, Eckert S, Gerbeth G (2013) Spin-up of a magnetically driven tornado-like vortex. *J Fluid Mech* 736:641–662.
42. Vogt T, Räbiger D, Eckert S (2014) Inertial wave dynamics in a rotating liquid metal. *J Fluid Mech* 753:472–498.
43. Shishkina O, Horn S (2016) Thermal convection in inclined cylindrical containers. *J Fluid Mech* 790:R3.

PNAS
www.pnas.org

Supplementary Information for

Jump Rope Vortex in Liquid Metal Convection

Tobias Vogt, Susanne Horn, Alexander M. Grannan, and Jonathan M. Aurnou

Tobias Vogt.
E-mail: t.vogt@hzdr.de

This PDF file includes:

Supplementary text
Figs. S1 to S4
Table S1
Captions for Movies S1 to S4

Other supplementary materials for this manuscript include the following:

Movies S1 to S4

www.pnas.org/cgi/doi/10.1073/pnas.1812260115

Supporting Information Text

Identifying the Jump Rope Vortex

The jump rope vortex leaves a characteristic imprint on several of the output parameters. It can be most easily identified using the azimuthally averaged sidewall temperature at midheight, T_{avg}, a quantity that is measured in most laboratory experiments. The jump rope vortex cases ($\Gamma = 2$ and $\Gamma = \sqrt{2}$) exhibit a T_{avg} signal with a regular oscillation at the characteristic frequency f_0 (see Fig. 5). In contrast, the T_{avg} signal in $\Gamma = 1$ has no clear oscillation. Instead, in $\Gamma = 1$ cases, it is the azimuthal LSC angle ξ_{LSC} that contains a strong oscillation.

The thermal signal of the jump rope can also be visualised in a space-time plot (Fig. 4*A*). We show 500 free-fall time units of circumferential midplane temperatures from liquid metal and water DNS in Fig. S3*A–D*, as well as magnifications in *E–H*. In addition, we present data for $Pr = 0.025$ in a $\Gamma = \sqrt{2}$ container for 100 free-fall time units in Fig. S4. The $\Gamma = 2$ and $\Gamma = \sqrt{2}$ data show an accordion-like pattern in both liquid metal and water (*E, G*), although this signal is, indubitably, far easier to identify in the low Pr metal. The $\Gamma = 1$ data shows a classical sloshing behaviour, i.e. the two extrema follow an in-phase zig-zag pattern (*F, H*), again with the clearer thermal signal in the thermally diffusive metal. Note that the path length of the jump rope vortex cycle is approximately $6H$, while the horizontal sloshing path length is only approximately $4R$, explaining the difference in the duration of the respective cycles for the jump roping $\Gamma = 2$ cases and the sloshing $\Gamma = 1$ cases.

We have verified with DNS that both identification methods, the averaged signal T_{avg} and the midplane sidewall patterns, can be used to detect jump rope or slosh modes using 8 probes uniformly placed around the circumference.

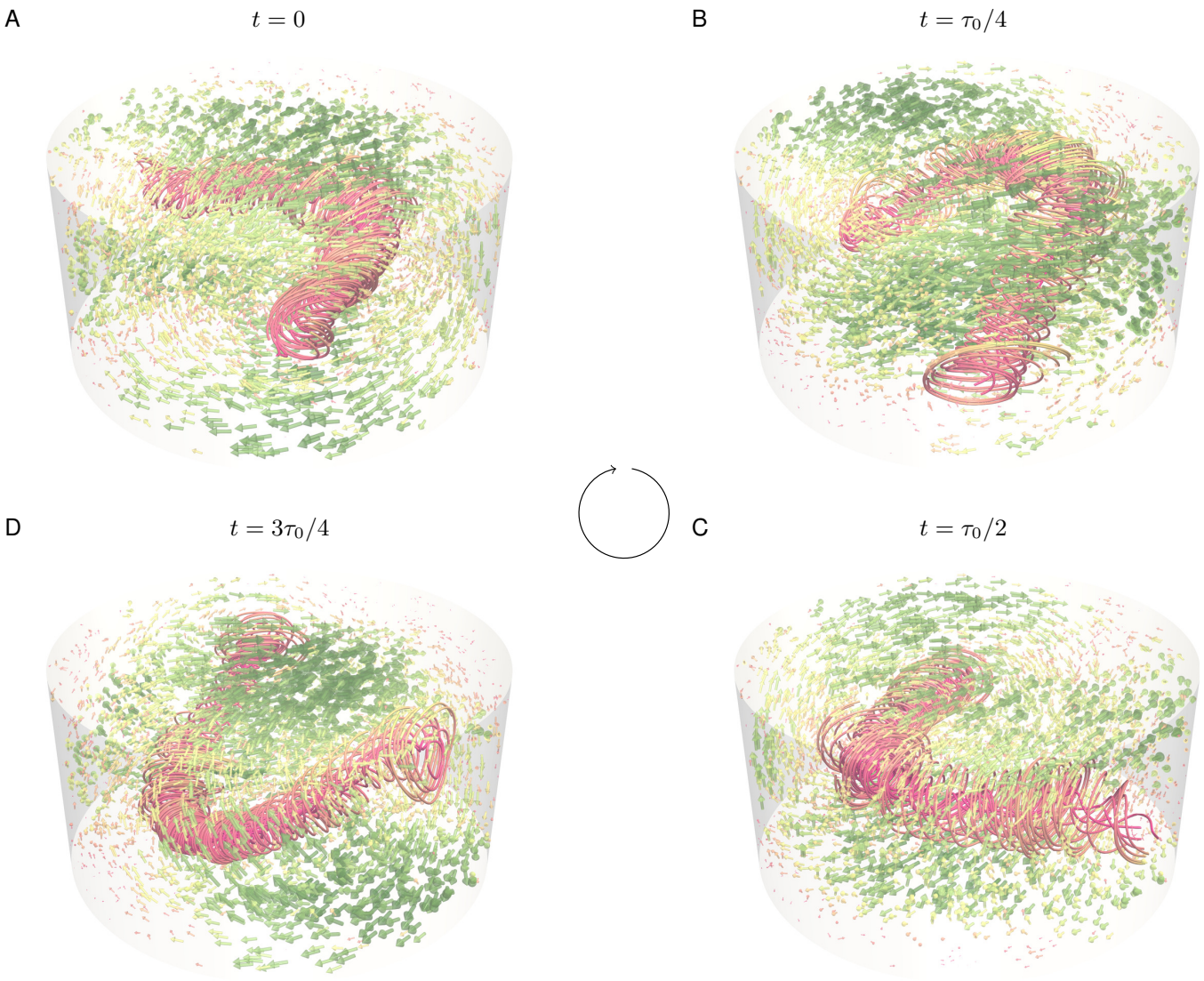

Fig. S1. Renderings of the LSC flow field and embedded jump rope vortex. The four panels are 3D representations of Fig. 1*B–D*. The vector arrows show the velocity field and are coloured and scaled in size by the magnitude $\|\vec{u}\|/u_{ff}$. The streamlines wrap around the jump rope vortex core. The colour scale is the same as in Fig. 1. The jump rope cycle is animated in the Supplementary Movies S3 and S4.

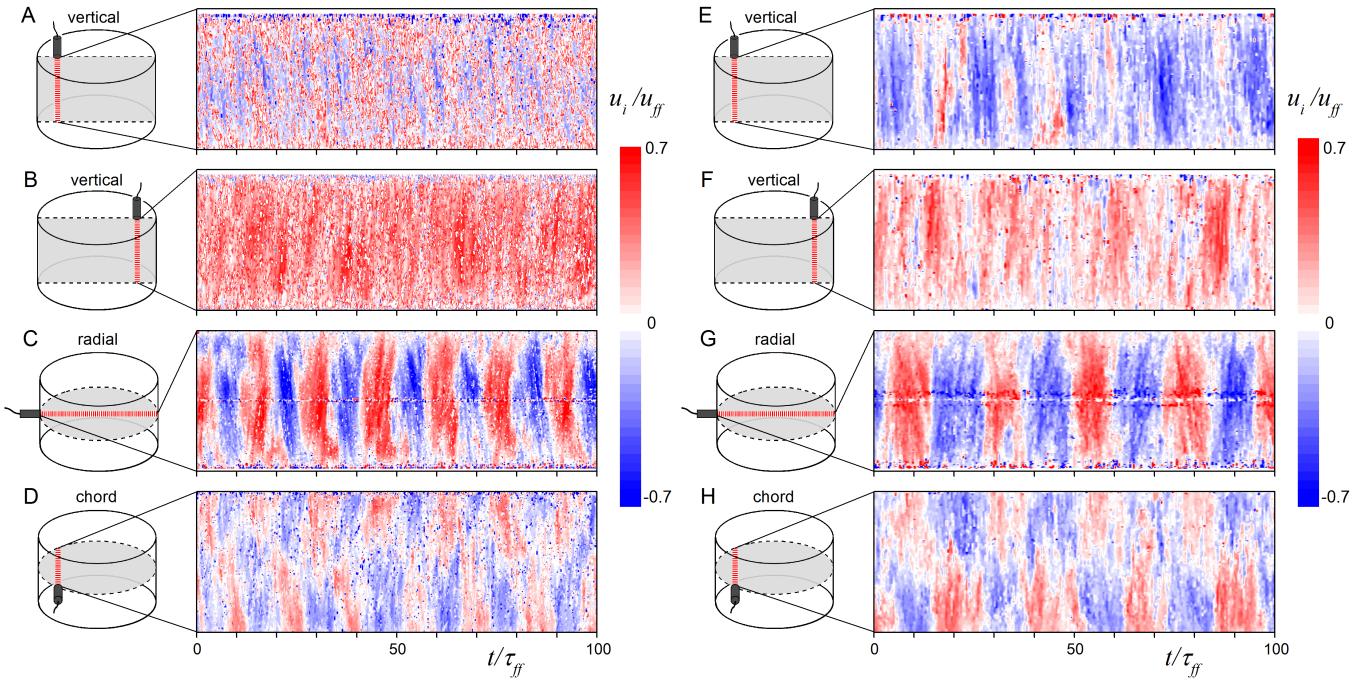

Fig. S2. Spatio-temporal evolution of laboratory convection velocities, similar to Fig. 3, from near the low and high ends of the investigated Rayleigh numbers. The left column (A–D) shows simultaneous ultrasonic Doppler measurements for $Ra = 7.05 \times 10^4$, $Pr = 0.028$, $\Gamma = 2$; the measurements are non-dimensionalised using the free-fall velocity $u_{ff} = \sqrt{\alpha g \Delta H} = 5.86\,\mathrm{mm/s}$ and the free-fall time $\tau_{ff} = H/u_{ff} = 16.79\,\mathrm{s}$. The right column (E–H) shows $Ra = 5.13 \times 10^6$, $Pr = 0.026$, $\Gamma = 2$, the measurements are non-dimensionalised with $u_{ff} = 48.29\,\mathrm{mm/s}$ and $\tau_{ff} = 2.04\,\mathrm{s}$. The particular measuring lines are indicated as a dashed red line in the schematics left of each data panel. Negative (positive) velocities represent flow away from (towards) the transducer. The ordinate corresponds to the measuring depth along the tank height (A, B) and (E, F), diameter (C, G), and chord (D, H), respectively. The measurements in (A–C) and (E–G) lie in the symmetry plane of the LSC; the chord probe measurements in (D, H) lie perpendicular to the LSC symmetry plane. The axial velocity in (A, E) and (B, F) show a mean down- and upflow, respectively, and relatively weak periodic fluctuations. While the mean velocity is zero in (C, G) and (D, H), strong oscillations are observed that span the tank. The flow along the chord in (D, H) shows a periodic double cell structure whereby the oscillation is in phase to (C, G).

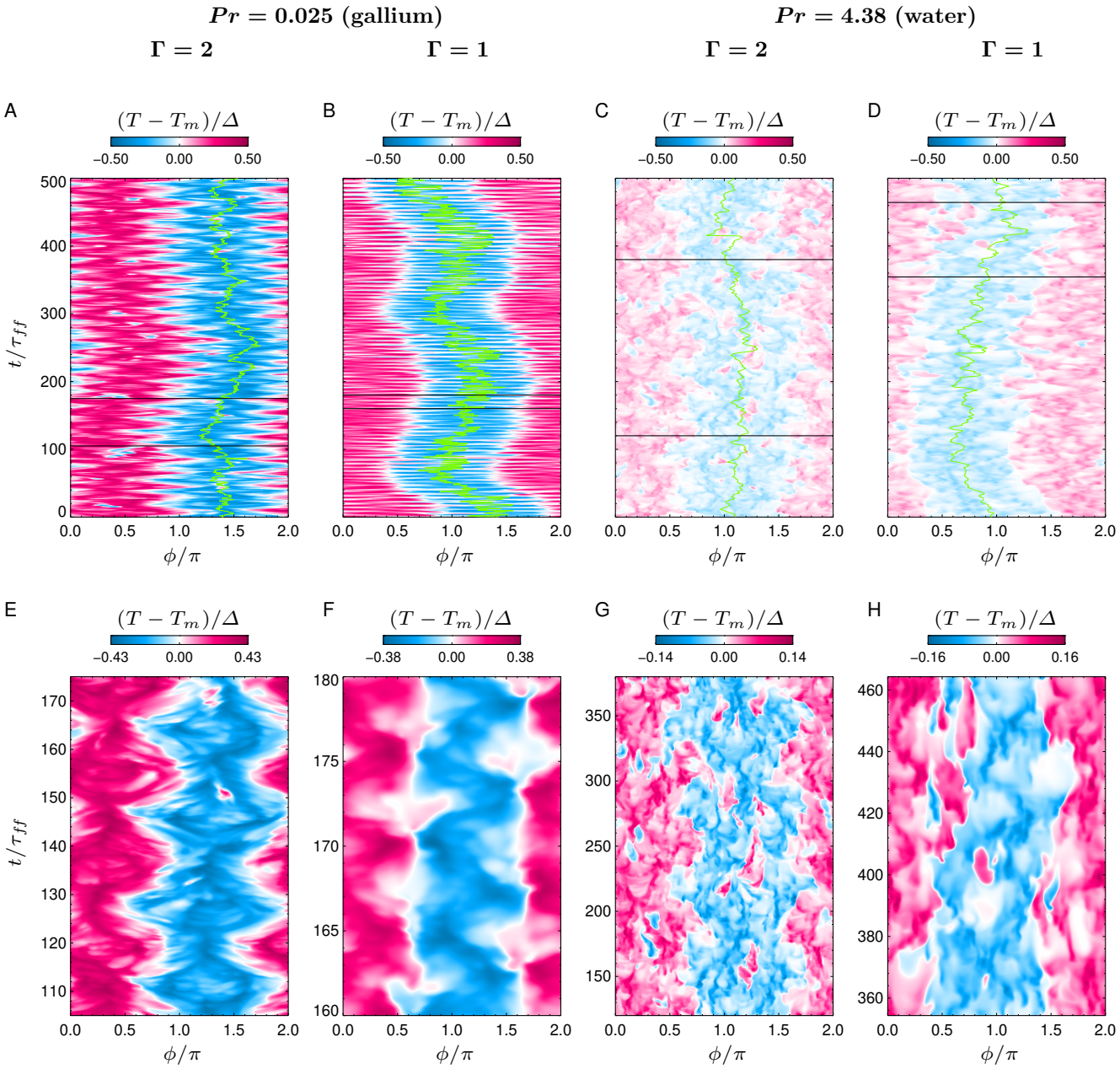

Fig. S3. Midplane sidewall temperature distribution for gallium and water DNS. The upper panels (A)–(D) show the sidewall thermal pattern over 500 free-fall times t/τ_{ff}. The green line marks the position of the LSC ξ_{LSC}. The colour scale covers the entire possible temperature range, -0.5 to $+0.5$. The lower panels (E)–(H) are magnifications of the areas indicated by black horizontal lines in the respective panels above, showing approximately four LSC cycles and using temperature ranges restricted to the interval $[-\max|(T - T_m/\Delta|), +\max|(T - T_m/\Delta)|]$ for each case. The left-hand figures correspond to gallium, $Pr = 0.025$, $Ra = 1.12 \times 10^6$, with (A, E) $\Gamma = 2$ and (B, F) $\Gamma = 1$. The right-hand figures correspond to water, $Pr = 4.38$, $Ra = 10^8$, with (C, G) $\Gamma = 2$ and (D, H) $\Gamma = 1$. Note, that water has a lower level of turbulence, that is $l_{coh}^{Ga}/H \approx 0.03$ and $Re_{r,rms}^{Ga} = 4789.9$ compared to $l_{coh}/H^{H_2O} \approx 0.09$ and $Re_{r,rms}^{H_2O} = 797.3$, whereas the Peclet number is significantly higher with $Pe^{Ga} = 121.7$ and $Pe^{H_2O} = 3492.2$, resulting in the visibly clearer temperature signal of gallium.

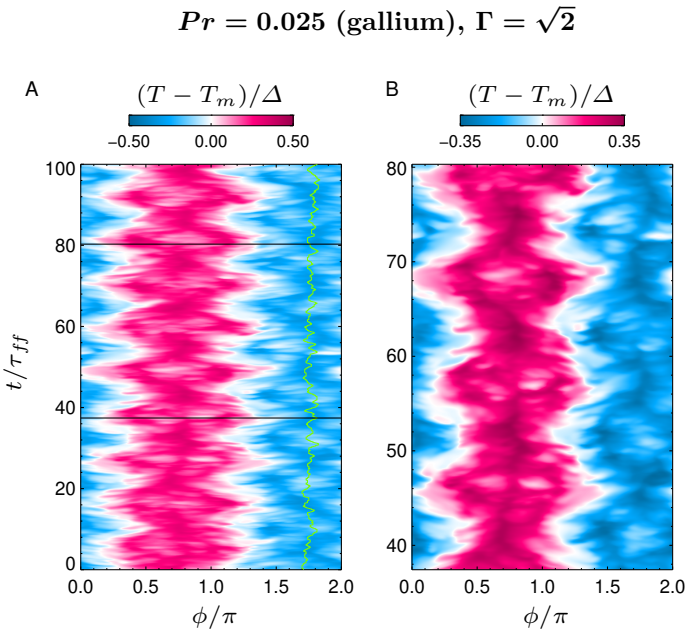

Fig. S4. Midplane sidewall temperature distribution for gallium with $Pr = 0.025$, $Ra = 1.12 \times 10^6$, and $\Gamma = \sqrt{2}$ shown for (A) 100 free-fall times t/τ_{ff} and (B) for approximately four LSC cycles, similar to Fig. S3.

Table S1. Data table for the conducted laboraty experiments. The first three columns show the dimensional control parameters, that are varied throughout the suite of experiments: the applied heating power P, the temperature drop Δ, the mean fluid temperature T_{mean}. The next two columns show the corresponding non-dimensional control parameters: the Prandtl and Rayleigh number Pr and Ra. Column six to eight show the frequencies obtained through the measured temperature spectra, f_0^T, and the radial velocity spectra, dimensional $f_0^{u_r}$ and in thermal diffusion time units, $H^2 f_0^{u_r}/\kappa$. The last three columns show the free-fall velocity u_{ff}, the measured rms value of the radial velocity $u_{r,rms}$ and the Reynolds number based on the latter, $Re_{r,rms}$. The cases presented in Fig. 2 and Fig. S2 are highlighted in bold.

P [W]	Δ [K]	T_{mean} [K]	Pr	Ra	f_0^T [Hz]	$f_0^{u_r}$ [Hz]	$f_0^{u_r} H^2/\kappa$	u_{ff} [mm/s]	$u_{r,rms}$ [mm/s]	$Re_{r,rms}$
7.31	0.30	35.67	0.0277	7.55×10^4	3.57×10^{-3}	3.52×10^{-3}	2.69	5.97	2.24	1.23×10^3
7.71	**0.28**	**35.69**	**0.0277**	$\mathbf{7.05 \times 10^4}$	$\mathbf{3.49 \times 10^{-3}}$	$\mathbf{3.61 \times 10^{-3}}$	**2.75**	**5.86**	**2.20**	$\mathbf{1.20 \times 10^3}$
13.77	0.47	35.89	0.0277	1.18×10^5	4.71×10^{-3}	4.71×10^{-3}	3.59	7.51	2.96	1.62×10^3
13.05	0.53	35.98	0.0277	1.34×10^5	4.81×10^{-3}	4.90×10^{-3}	3.74	7.97	3.05	1.68×10^3
25.62	0.78	36.22	0.0277	1.97×10^5	5.93×10^{-3}	5.96×10^{-3}	4.55	9.70	3.86	2.12×10^3
26.88	0.86	36.37	0.0277	2.17×10^5	5.89×10^{-3}	6.20×10^{-3}	4.73	10.17	3.64	2.00×10^3
53.29	1.33	36.98	0.0276	3.37×10^5	7.60×10^{-3}	7.73×10^{-3}	5.90	12.68	4.95	2.73×10^3
53.26	1.34	36.97	0.0276	3.39×10^5	7.74×10^{-3}	7.68×10^{-3}	5.86	12.73	4.71	2.60×10^3
53.27	1.33	36.97	0.0276	3.37×10^5	7.67×10^{-3}	7.66×10^{-3}	5.84	12.69	4.80	2.65×10^3
53.33	1.35	36.98	0.0276	3.42×10^5	7.66×10^{-3}	7.71×10^{-3}	5.88	12.75	4.92	2.72×10^3
99.15	2.33	38.21	0.0274	5.93×10^5	9.63×10^{-3}	9.57×10^{-3}	7.30	16.76	6.37	3.54×10^3
100.40	2.28	38.23	0.0274	5.81×10^5	9.62×10^{-3}	9.54×10^{-3}	7.28	16.60	6.02	3.34×10^3
203.73	3.88	40.59	0.0271	9.99×10^5	1.20×10^{-2}	1.18×10^{-2}	9.00	21.65	7.54	4.23×10^3
199.50	3.85	40.56	0.0271	9.91×10^5	1.18×10^{-2}	1.17×10^{-2}	8.92	21.54	7.97	4.47×10^3
199.82	3.86	40.51	0.0271	9.94×10^5	1.17×10^{-2}	1.17×10^{-2}	8.89	21.59	7.80	4.38×10^3
209.12	**3.99**	**41.72**	**0.0269**	$\mathbf{1.03 \times 10^6}$	$\mathbf{1.19 \times 10^{-2}}$	$\mathbf{1.20 \times 10^{-2}}$	**9.12**	**21.95**	**8.35**	$\mathbf{4.72 \times 10^3}$
426.64	6.95	45.66	0.0264	1.83×10^6	1.48×10^{-2}	1.47×10^{-2}	11.21	28.96	10.68	6.15×10^3
426.60	6.92	45.65	0.0264	1.82×10^6	1.46×10^{-2}	1.46×10^{-2}	11.14	28.90	11.26	6.48×10^3
426.37	6.93	45.65	0.0264	1.83×10^6	1.50×10^{-2}	1.50×10^{-2}	11.44	28.92	10.87	6.25×10^3
792.94	11.37	41.20	0.0270	2.94×10^6	1.78×10^{-2}	1.81×10^{-2}	13.81	37.04	12.95	7.29×10^3
792.09	11.35	41.26	0.0270	2.93×10^6	1.82×10^{-2}	1.78×10^{-2}	13.58	37.01	12.73	7.17×10^3
1579.51	**19.32**	**47.10**	**0.0262**	$\mathbf{5.13 \times 10^6}$	$\mathbf{2.22 \times 10^{-2}}$	$\mathbf{2.20 \times 10^{-2}}$	**16.78**	**48.29**	**15.99**	$\mathbf{9.27 \times 10^3}$
1579.58	19.36	47.28	0.0262	5.14×10^6	2.22×10^{-2}	2.19×10^{-2}	16.71	48.33	16.46	9.55×10^3

Movie S1. Temperature and velocity vectors of the full DNS at $Pr = 0.025$, $Ra = 1.12 \times 10^6$, $\Gamma = 2$. The time is reported in free-fall time units τ_{ff} and the temperature is scaled as $(T - T_m)/\Delta$. The left circular panel shows the temperature in the midplane. The green line marks the LSC symmetry plane ξ_{LSC} and the orange line lies in the perpendicular plane $\xi_{LSC} + \pi/2$. Vertical cross-sections defined by those planes are shown in the right panels.

Movie S2. Conditionally-averaged temperature fields constructed using the data shown in Supplementary Movie 1, but extending out to $t/\tau_{ff} = 1000$. Note that the jump rope vortex core, shown in the upper right panel, moves opposite to the mean circulation visualised by the velocity vectors.

Movie S3. Jump rope vortex. The upper panel is colour-coded with the velocity magnitude as in Fig. 1. The lower panel shows the same streamlines and line-integral convolution (LIC) method as in the upper panel, but the colour scale corresponds to the temperature. In addition, the sidewall temperature field is displayed on the back half of the cylinder.

Movie S4. Jump rope vortex renderings in oblique (left), top (center) and side view (right). The vector arrows show the velocity field and are colored and scaled in size by the magnitude $\|\vec{u}\|/u_{ff}$. The streamlines wrap around the jump rope vortex core. The colour scale is the same as in Fig. 1.